Xu *et al. Soft Sci.* **2025**, *5*, 43
DOI: 10.20517/ss.2025.63

Soft Science

Research Article

Open Access

Check for updates

Bioinspired porous Ti_2CT_X/Si_3N_4 composites with aligned lamellar structure for efficient microwave absorption

Hailong Xu[1], Chenyang Jing[1], Zhijian Xu[1], Haoyang Zhan[1], Fang Ye[1], Qiang Chen[1], Meng Zhu[2,*], Luo Kong[3], Xinliang Li[4], Xia Chai[5], Yuchang Qing[1], Xiaomeng Fan[1,*], Fa Luo[1]

[1]School of Materials Science and Engineering, Northwestern Polytechnical University, Xi'an 710072, Shaanxi, China.
[2]College of Bioresources Chemical & Materials Engineering, Shaanxi University of Science &Technology, Xi'an 710021, Shaanxi, China.
[3]School of Materials Science and Engineering, Shaanxi Key Laboratory of Green Preparation and Functionalization for Inorganic Materials, Shaanxi University of Science and Technology, Xi'an 710021, Shaanxi, China.
[4]School of Physics and Laboratory of Zhongyuan Light, Zhengzhou University, Zhengzhou 450052, Henan, China.
[5]Shaanxi Huaqin Technology Industry Co., Ltd. Xi'an 710119, Shaanxi, China.

[*]**Correspondence to:** Assoc. Prof. Xiaomeng Fan, School of Materials Science and Engineering, Northwestern Polytechnical University, Xi'an 710072, Shaanxi, China. Email: fanxiaomeng@nwpu.edu.cn; Assoc. Prof. Meng Zhu, College of Bioresources Chemical & Materials Engineering, Shaanxi University of Science &Technology, Longshuo Road, Weiyang University Park, Xi'an 710072, Shaanxi, China. Email: mengzhu@sust.edu.cn

How to cite this article: Xu, H.; Jing, C.; Xu, Z.; Zhan, H.; Ye, F.; Chen, Q.; Zhu, M.; Kong, L.; Li, X.; Chai, X.; Qing, Y.; Fan, X.; Luo, F. Bioinspired porous Ti_2CT_X/Si_3N_4 composites with aligned lamellar structure for efficient microwave absorption. *Soft Sci.* **2025**, *5*, 43. https://dx.doi.org/10.20517/ss.2025.63

Received: 30 Jul 2025 **First Decision:** 20 Aug 2025 **Revised:** 24 Aug 2025 **Accepted:** 28 Aug 2025 **Published:** 8 Sep 2025

Academic Editor: YongAn Huang **Copy Editor:** Shu-Yuan Duan **Production Editor:** Shu-Yuan Duan

Abstract

With the ever-deepening understanding of nano-electromagnetic interactions and the advancements of fabrication methodologies of nanomaterials, diverse electromagnetic platforms utilizing nanomaterials have been developed for next-generation electromagnetic safeguarding applications. This study presents the design and fabrication of bioinspired porous Ti_2CT_X/Si_3N_4 composites featuring an aligned lamellar structure, aimed at facilitating the effective absorption and dissipation of electromagnetic radiation. The layered configuration of Ti_2CT_X/Si_3N_4 composites facilitates the repeated reflection of electromagnetic waves between neighboring Ti_2CT_X layers, hence enhancing the energy dissipation of these waves. At a Ti_2CT_X concentration of merely 0.21 wt.%, the effective absorption bandwidth of Ti_2CT_X/Si_3N_4 composites encompasses the whole X-band (8.2-12.4 GHz), with a minimum reflection loss of -53 dB achievable at a sample thickness of 5 mm. Simultaneously, the fabricated Ti_2CT_X/Si_3N_4 composites demonstrate advantages in lightweight characteristics and robust mechanical properties, offering significant insights for the application of Ti_2CT_X in nano-electromagnetic engineering, particularly in the

realm of electromagnetic pollution mitigation.

Keywords: Ti_2CT_X, amorphous Si_3N_4, bio-inspired lamellar structure, ice-templated method, microwave absorption

INTRODUCTION

Over the past 20 years, the integration of nanomaterials with dielectrics and electromagnetic fields has flourished[1,2], achieving remarkable accomplishments across various domains. Among these, nano-functional materials applied to protect against gigahertz (GHz) electromagnetic wave pollution have emerged as a hot topic in research and applications[3-6]. With the continuous advancement of technology[7], the increasing popularity of electronic devices and their higher operating frequencies and power levels have led to an increase in the severity of GHz electromagnetic wave pollution[8,9]. This poses a significant threat to both human health and the normal functioning of electronic devices[10-14]. Electromagnetic wave absorbing materials could eliminate electromagnetic pollution based on absorption, and the electromagnetic energy can be directly converted into non-polluting energy, such as heat[15], thus avoiding the secondary pollution of electromagnetic waves. To meet the diverse needs of practical applications, electromagnetic wave-absorbing materials must have good mechanical properties and functionality.

Natural materials owe their unique performance not merely to their intrinsic chemistry but to ingenious structural design that orchestrates interactions among constituents. Today, macro-, micro-, and nano-scale architectures are engineered to unlock a material's full potential[16-20]. For example, the human skull consists of two layers: a dense layer of bone and a loose porous cancellous bone layer[21]. This layer has a three-dimensional (3D) porous sandwich structure and good compressive strength[22-24]. This is sufficient to protect the brain from external loads during daily human activities. The porous structure of plants plays a vital role in transporting nutrients[25], providing mechanical support and regulating the transpiration process[26] and replicating moth eyes to introduce gradual transitions that prevent abrupt impedance jumps and enable broad-band impedance matching[27]. By sculpting intricate 3D geometries - porous networks, honeycombs, foams, and labyrinthine channels - electromagnetic waves are forced to undergo multiple reflections, scattering, and diffraction inside the material, greatly extending their propagation paths and dissipating their energy[28,29]. The integrative nature of natural materials - simultaneously providing electromagnetic absorption, mechanical load-bearing, and lightweight characteristics - offers a blueprint for architecting materials across micro- and macro-scales, opening new avenues for electromagnetic-wave-absorbing materials.

MXene is a new type of two-dimensional (2D)[30,31], layered, transition-metal-based material with a unique physical structure that can be used to produce electromagnetic wave-absorbing composite materials[32-34]. First, the surface of MXene is abundant in functional groups (e.g., -OH, -O, -F)[35]. These functional groups generate dipole polarization in the presence of an electromagnetic field, enhancing the dielectric loss capability of the material[36]. Furthermore, MXene can self-assemble into 3D porous structures under the influence of electrostatic and van der Waals forces[37]. Secondly, MXenes have high electrical conductivity[38], enabling the formation of an effective conductive network and improving the conductive loss. Third, its 2D layered structure can effectively enhance the multiple reflections and scattering of electromagnetic waves within the material[39], thereby improving its absorption efficiency[40-42]. Therefore, assembling 2D MXenes into 3D structures can effectively enhance electromagnetic wave absorption performance. Zhao *et al.* blended graphene oxide with an MXene suspension and coated MXene nanosheets onto the surface of a reduced graphene oxide (rGO) skeleton[43]. This process yielded MXene/rGO hydrogels that were freeze-dried to create a 3D porous structure, with shielding effectiveness of more than -50 dB in

the X-band at a low $Ti_3C_2T_X$ content of 0.74 vol.%. However, the large specific surface area and high number of surface functional groups make MXenes highly susceptible to oxidation in air. The poor compressive ability and insufficient mechanical properties of MXene aerogels are greatly limited by their inherent brittleness, 2D lamellar structure, and lack of a protective layer. The researchers found that the oxidation of MXenes could be effectively prevented, and their stability improved through compositing with other materials and structural design. Wu *et al.* reported on an MXene/MoS_2 composite coated with carbon to protect its structure[44]. This carbon layer reduces oxidation by external oxygen and the formation of oxygen-containing groups during annealing at high temperatures. Zhao *et al.* reported that an MXene/GO-based aerogel possesses structural diversity and an outstanding electromagnetic interference (EMI) shielding effectiveness of > -50 dB[43]. All of the abovementioned second-phase materials are highly conductive[45]. The introduction of these materials affects the dielectric properties of the substrate, making it difficult to regulate these properties. This increases the reflection of electromagnetic waves on the surface of the material, thereby reducing its absorption efficiency. In contrast, introducing electromagnetic wave transparent materials with lower dielectric constants does not affect the dielectric properties of the substrate material but can improve its stability to a certain extent. Si_3N_4 is characterized by its low density (3.18-3.44 g/cm^3), excellent microwave transparent dielectric properties[46], and good mechanical and chemical stabilities[47,48]. Therefore, it can maintain structural integrity in extremely harsh environments and is not easily deformed or damaged. Its low dielectric loss helps reduce the reflection of electromagnetic waves on the material surface[49-51], allowing the electromagnetic waves to pass through effectively and reach deep inside the material. Amorphous Si_3N_4 prepared by Chemical Vapor Infiltration (CVI) has several unique advantages[52,53], including (1) Structural homogeneity: Amorphous Si_3N_4 has no long-range ordering and does not have structural defects such as grain boundaries, twins, and dislocations; (2) Excellent mechanical properties: amorphous Si_3N_4 are stronger and harder than crystalline Si_3N_4, making them suitable for high-strength and high-toughness applications; (3) Chemical stability: amorphous Si_3N_4 is chemically stable and has good antioxidant properties, enabling it to remain stable in high-temperature and oxidative environments. Therefore, depositing amorphous Si_3N_4 on the surface of MXene using the CVI process results in a uniformly distributed Si_3N_4 layer, forming a unique Si_3N_4-MXene-Si_3N_4 sandwich structure[54]. This effectively improved the mechanical properties and chemical stability of the aerogel. Overall, a Si_3N_4-MXene composite aerogel with a layered porous structure is expected to enhance both the mechanical and electromagnetic wave absorbing properties simultaneously; however, there are currently few related studies.

Here, we provide new ideas for nanomaterials in the field of electromagnetic wave absorption by introducing insulating electromagnetic wave transparent materials in combination with MXene's properties. In this study, MXene aerogel with lamellar structure was fabricated via a bidirectional freeze-drying method. Then we deposited amorphous Si_3N_4 onto the surface of MXene nanosheets of Ti_2CT_X aerogels using the CVI technique[55]. The resulting Ti_2CT_X/Si_3N_4 composites retained the pristine lamellar structure of MXene aerogel. The layered porous structure of the Ti_2CT_X/Si_3N_4 aerogel promotes multiple reflections and scattering of electromagnetic waves within the material, which significantly increases the propagation path of electromagnetic waves, thereby improving the opportunity for absorption. In addition, the combination of the high electrical conductive MXenes and the low dielectric Si_3N_4 produces interfacial polarization, the abundance of functional groups on the surface of MXene brings sufficient dipole polarization, the high electrical conductivity of MXene given conductive loss, the synergistic effect of the multiple reflections and scattering, interfacial polarization, dipole polarization, and conductive loss results in an efficient electromagnetic wave absorption system[56]. With a Ti_2CT_X content of only 0.21 wt.%, the composites have an effective absorption bandwidth (EAB) that covers the entire X-band (8.2-12.4 GHz). The lowest reflection loss of –53 dB was achieved at a sample thickness of 5 mm. Therefore, this study proposes the design and fabrication of biomimetic porous Ti_2CT_X/Si_3N_4 composites with a laminated structure to effectively absorb and dissipate electromagnetic radiation.

METHODS

Materials

Ti_2AlC powders were purchased from Lianlixin Technology Co., Ltd., China. Lithium fluoride (LiF) and hydrochloric acid (HCl) solution were obtained from Aladdin Reagent. Silicon tetrachloride ($SiCl_4$ ≥ 99.99%), ammonia (NH_3 ≥ 99.99%), Hydrogen (H_2 ≥ 99.99 %), and argon (Ar ≥ 99.9%) were obtained from Xian Wei Guang Gas Co., Ltd. All compounds were utilized immediately without additional purification unless otherwise indicated.

Preparation of few-layered Ti_2CT_X nanosheets

Few-layered Ti_2CT_X nanosheets were synthesized by selectively removing aluminum atoms from Ti_2AlC powders using an etching solution. The etchant was formulated by dissolving 1.0 g of LiF in 30 mL of 10 M HCl, resulting in a homogeneous acidic solution for subsequent etching reactions. The preparation procedure commenced with the gradual addition of Ti_2AlC powder into the etchant solution under constant magnetic stirring. The resultant mixture was subjected to continuous agitation at ambient temperature for 72 h to facilitate complete etching. Subsequently, the etched powder underwent multiple centrifugation cycles (5 min per cycle at 6,000 rpm) using deionized (DI) water until a neutral pH of 6.5 was attained. The purified sediment was vacuum-dried for 72 h, and the final dried powder was kept until further use.

Preparation of porous Ti_2CT_X/Si_3N_4 composites

The porous Ti_2CT_X aerogel with an aligned lamellar structure was prepared via a bidirectional freezing method. The homemade Teflon tubes (23 mm × 11 mm × 30 mm) were sealed with a copper plate and a polydimethylsiloxane (PDMS) wedge titled to an angle of 20°. Ti_2CT_X slurry with a concentration of 10 mg/mL was poured into the mold and then frozen in liquid nitrogen. The frozen samples were put in a vacuum freeze dryer to move the ice template for 36 h under 0.1 Pa pressure. Then the porous Ti_2CT_X/Si_3N_4 composite was fabricated by infiltrating Si_3N_4 into the obtained Ti_2CT_X foams at 1,073 K in a chemical vapor infiltration furnace with a gaseous atmosphere of $SiCl_4$-NH_3-H_2-Ar system, the deposition parameters of $SiCl_4$-NH_3-H_2-Ar system in Supplementary Table 1. The specific constituents comprised silicon tetrachloride as the silicon source, ammonia as the nitrogen source, and hydrogen as the dilution gas. Ti_2CT_X/Si_3N_4 composites were obtained after the entire chemical vapor infiltration procedure was completed. The chemical reaction is as follows [57]:

$$3SiCl_4(g)+4NH_3(g) \xrightarrow{H_2} Si_3N_4(s)+12HCl(g)$$

Simulation calculation

The model has a thickness of 5 mm in the Z-axis using the Microwaves & RF/Optical module in CST Studio Suite 2020, with the material set to MXene from the material library. Periodic boundary conditions are set in the XY-axis. A perfectly matched layer is set in the Z-axis direction and a perfectly conductive layer is set in the Z-axis. The incident electromagnetic wave is directed along the Z axis, and calculations are performed at 8.2, 10.3, and 12.4 GHz to determine current density, E, power flow, and power loss density.

Characterization

The X-ray diffractometer (X'Pert Pro, Philips, Netherlands) confirmed the microstructure of samples, while morphology was characterized on a scanning electron microscope (SEM, HITACHI S-4700, Japan) and a transmission electron microscope (TEM, G20, FEI Tecnai, USA). The thermal stability of Ti_2CT_X and Ti_2CT_X/Si_3N_4 was measured in ambient air and argon respectively by a thermogravimetric analyzer (TGA, STA449F3, Netzsch) from 30 to 1,200 °C.

Ti_2CT_X and Ti_2CT_X/Si_3N_4 composites for microwave absorption testing were tailored and refined into samples of 22.86 mm × 10.16 mm × x mm in dimension, and their dielectric constant was measured by the waveguide method on a vector network analyzer (VNA, MS4644A, Anritsu, Japan) through the waveguide method in a frequency range corresponding to the X-band (8.2-12.4 GHz). The calculation of reflection coefficient (RC) in decibels (dB) was based on the measured EM parameter values referring to a metal back-panel model as follows:

$$RC = 20\log_{10}\left|\frac{Z_{in}-1}{Z_{in}+1}\right|$$

$$Z_{in} = \sqrt{\frac{\mu}{\varepsilon}}\tan h\left(j2\pi\sqrt{\mu\varepsilon}fd/c\right)$$

where c is the speed of light in vacuum, f is the frequency, ε is the dielectric constant, μ is permeability, and d is the thickness of samples.

RESULTS AND DISCUSSION

Fabrication and characterization of Ti_2CT_X/Si_3N_4 composites

Simulation tests have shown that the layered biomimetic structure designed in this study offers significant advantages for electromagnetic wave absorption. Firstly, two different structural models were designed: a bidirectionally oriented biomimetic multilayer structure [Figure 1A(1)] and a unidirectionally oriented porous structure [Figure 1B(1)]. When electromagnetic waves are incident along the Z-axis, we can observe the distribution of power loss density within a material, and assess its absorption performance of electromagnetic waves. The greater the power loss density, the faster the electromagnetic waves are lost. Through simulation calculations, the maximum values of the layered biomimetic structure at 8.2, 10.3, 12.4 GHz are 1.0×10^8, 1.3×10^8, 1.4×10^8 [Figure 1A(2)-A(4)]. The maximum values of the porous structure at 8.2, 10.3, and 12.4 GHz are 1.1×10^7, 1.5×10^7, and 1.7×10^7, respectively [Figure 1B(2)-B(4)]. Compared with unidirectional porous structures, layered biomimetic structures can dissipate electromagnetic waves more effectively. To further illustrate the advantages of layered biomimetic structures, comparisons were made between current density, E and power flow [Figure 1C-E]. The images show that bidirectional layered biomimetic structures have significant advantages, as they can dissipate electromagnetic waves more efficiently and reduce electromagnetic wave reflection. Therefore, we chose a bidirectional, layered, biomimetic structure for our design and prepared Ti_2CT_X/Si_3N_4 composite materials.

The preparation process is shown in Figure 2 preparation of Ti_2CT_X aerogel: (1) Ti_2CT_X nanosheets were prepared by selectively removing Al atoms from Ti_2AlC powders using an etching solution. The etched powders were then subjected to multiple centrifugation cycles using DI water. Then, the purified precipitates were vacuum-dried for 72 h, and the dried powders were stored for next use; (2) involved the preparation of the Ti_2CT_X aerogel: Ti_2CT_X solution with a concentration of 10 mg/mL was poured into a mold, which was then frozen in liquid nitrogen. The frozen samples were placed in a vacuum freeze dryer, and the ice template was subjected to a pressure of 0.1 Pa for 36 h, resulting in the preparation of porous Ti_2CT_X aerogels with an ordered lamellar structure [Figure 2A]. Preparation of Ti_2CT_X/Si_3N_4 composites [Figure 2B]: Ti_2CT_X/Si_3N_4 composites were prepared by introducing Si_3N_4 into the Ti_2CT_X aerogel via the CVI in a gaseous $SiCl_4$-NH_3-H_2-Ar atmosphere at 1,037 K.

An optical image of the Ti_2CT_X/Si_3N_4 aerogel used for dielectric testing is presented in Figure 3A; the aerogel dimensions were 22.86 mm in length and 10.16 mm in width. The microstructure of the freeze-dried Ti_2CT_X aerogel showed a lamellar structure with orderly stacking of layers and an interlamellar spacing of about 30 μm [Figure 3B and Supplementary Figure 1]. A closer view of the lamellar structure revealed that the

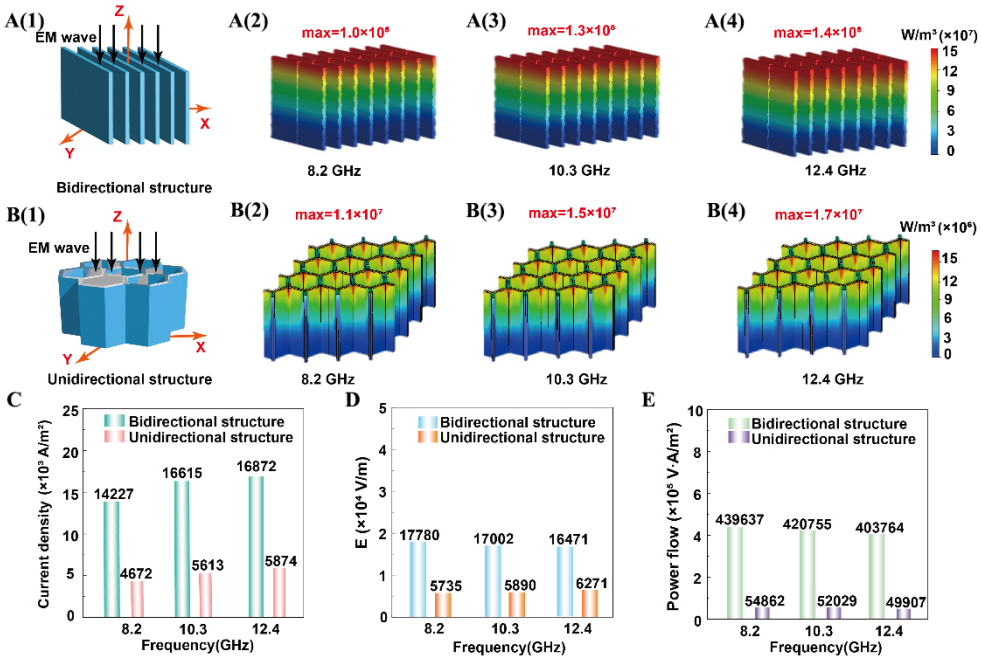

Figure 1. Structure design of Ti_2CT_X/Si_3N_4 composites. (A1) The Bidirectional structure; (A2-A4) CST simulation results for Power loss density of Bidirectional structure at 8.2-12.4 GHz; (B1) The Unidirectional structure; (B2-B4) CST simulation results for Power loss density of Unidirectional structure at 8.2-12.4 GHz; (C) Current density in CST simulations of different structures; (D) E in CST simulations of different structures; (E) Power flow in CST simulations of different structures.

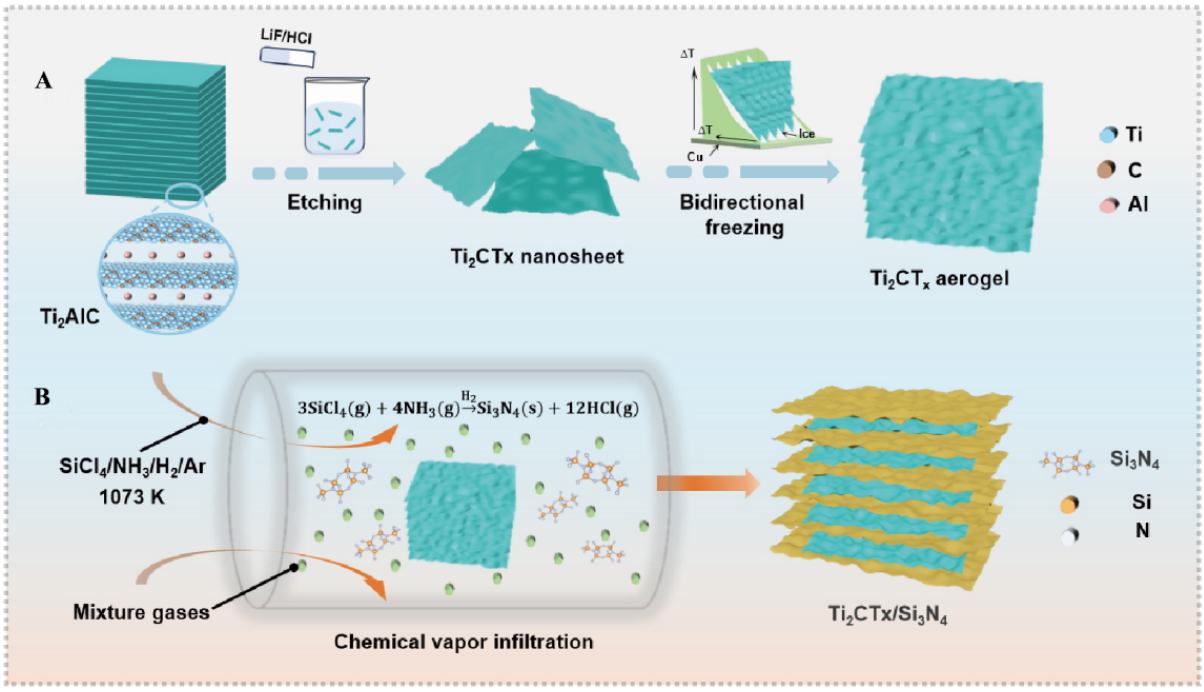

Figure 2. Schematic illustration of the fabrication route for Ti_2CT_X/Si_3N_4 composites.

spacing between the Ti_2CT_X lamellae decreased to approximately 23 μm after Si_3N_4 deposition [Supplementary Figure 2]. After the introduction of Si_3N_4, the surfaces of the Ti_2CT_X lamellae became

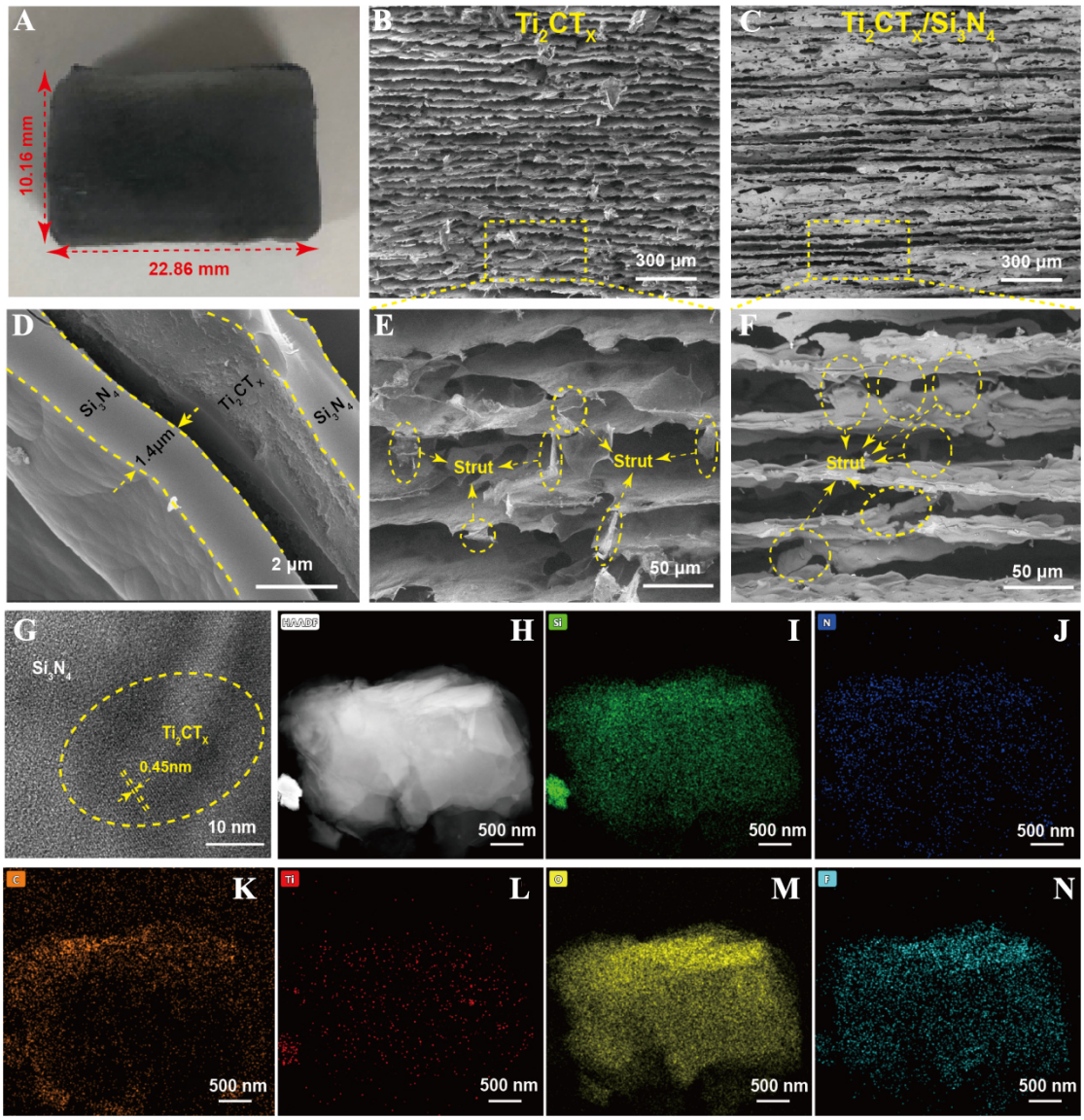

Figure 3. Microstructure characterization of Ti_2CT_X and Ti_2CT_X/Si_3N_4 aerogel. (A) Image of Ti_2CT_X/Si_3N_4 sample; (B) SEM image of pure Ti_2CT_X; (C) SEM image of Ti_2CT_X/Si_3N_4; (D) Cross-sectional SEM image of Ti_2CT_X/Si_3N_4; (E) SEM image of Ti_2CT_X; (F) SEM image of Ti_2CT_X/Si_3N_4; (G-N) EDS maps of Ti_2CT_X/Si_3N_4. SEM: Scanning electron microscope; EDS: energy dispersive X-ray spectroscopy; HAADF: high-angle annular dark-field.

rougher [Figure 3C and Supplementary Figure 3]. Guided by the quarter-wavelength theory, after Si_3N_4 incorporation the interlayer spacing shrinks from 30 μm to 23 μm. This reduction increases the effective propagation path, satisfying the λ/4 condition around 10 GHz and thereby intensifying multiple internal reflections and attenuation[58]. The smaller spacing also enlarges the distributed capacitance between adjacent Ti_2CT_X sheets, enhancing interfacial polarization and dielectric loss through stronger capacitive coupling. Simultaneously, the Si_3N_4 layer lowers the local effective permittivity near the surface while narrowing the spacing, improving impedance matching and allowing more electromagnetic energy to penetrate the material. The thickness of the Si_3N_4 layer was determined to be 1.4 μm at the Ti_2CT_X/Si_3N_4 cross-section [Figure 3D]. The formation of the Si_3N_4-Ti_2CT_X-Si_3N_4 sandwich structure was clearly observed. This structure reduces the reflection of electromagnetic waves through progressive impedance matching. A closer examination of the Ti_2CT_X microstructure revealed interconnected pillars between the layers. These

pillars provide the aerogel with good compressive strength when subjected to external pressure and strengthen the stability of the lamellar structure, preventing collapse [Figure 3E]. A porous structure composed of strut-like links was observed [Figure 3F], which increased the propagation paths of the electromagnetic waves. The synergistic effect of the two materials improves the electromagnetic wave absorbing efficiency of the material and confers lightweight and high strength.

In the TEM image of the Ti_2CT_X/Si_3N_4 aerogel [Figure 3G], a lattice spacing of 0.45 nm can be observed. From the elemental distribution characteristics of the Ti_2CT_X/Si_3N_4 aerogel surface, which correspond to the high-angle annular dark-field (HAADF) image [Figure 3H], it can be concluded that the main elements are Si, N, Ti, C, O, and F [Figure 3I-N, Supplementary Figure 4 and Supplementary Table 2]. The Ti and C elemental signals can still be detected following the introduction of Si_3N_4, suggesting that the original Ti_2CT_X was not destroyed by the addition of Si_3N_4. The weak signals of Ti and C elements are due to the masking of the elemental signals by the Si_3N_4 layer. The elements O and F are derived from the surface functional groups of Ti in Ti_2CT_X: O from the -OH group and F from the LiF used in the etching process. Based on the above analyses, it is shown that Si_3N_4 is successfully deposited by the CVI process on the surface of Ti_2CT_X, which is uniformly distributed and tightly wrapped around the Ti_2CT_X nanosheets.

The successful preparation of the Ti_2CT_X/Si_3N_4 aerogel was further demonstrated by X-ray diffraction (XRD) [Figure 4A], at 7.07° and 39.6°, corresponding to Ti_2CT_X (002) and (103) crystal planes, respectively. A comparison of the two XRD curves reveals that, following the introduction of Si_3N_4, a wide, flat scattering peak appears at 27.5°. The presence of the 'bun peak' confirms the successful introduction of amorphous Si_3N_4 through CVI. The XPS spectra indicate the presence of Si, N, C, Ti, O elements [Figure 4B]. There are two peaks in the Si 2p curve, at 100.1 eV and 101.01 eV, attributed to Si-O and Si-N bonds, respectively [Figure 4C]. There are two peaks in the N 1s curve, at 398.4 eV and 400.61 eV, which correspond to N-Si and N-C bonds, respectively, and are mainly in the form of N-Si bonds [Figure 4D]. We can see four peaks clearly in the C 1s curve, 284.85 eV corresponds to C-C, 286.75 eV corresponds to C-O-C, 288.54 eV corresponds to C=C and 290.06 eV corresponds to C-C=O [Figure 4E]. There are four peaks in the Ti 2p curve, 453.72 eV corresponds to $Ti^{3+}2p_{3/2}$, 457.02 eV corresponds to $Ti^{4+}2p_{3/2}$, 459.8 eV corresponds to $Ti^{3+}2p_{1/2}$, and 462.2 eV corresponds to $Ti^{4+}2p_{1/2}$ [Figure 4F]. These results indicate the successful preparation of the Ti_2CT_X/Si_3N_4 aerogel.

Dielectric properties and microwave absorption performance

The properties of electromagnetic wave-absorbing materials are described using electromagnetic parameters, including complex permittivity ($\varepsilon_r = \varepsilon' - j\varepsilon''$) and complex permeability ($\mu_r' = \mu' - j\mu''$)[59,60]. The real and imaginary parts of the dielectric constant reflect the stored and lost energy of the electromagnetic wave, respectively. We tested and compared the electromagnetic parameters of two structures: a biomimetic layered structure [Figure 5A(1)] and a porous structure [Figure 5B(1)] at 8.2-12.4 GHz. The dielectric constant ($\varepsilon_r = \varepsilon' - j\varepsilon''$) was measured to demonstrate dielectric properties within the frequency range of 8.2-12.4 GHz [Figure 5A(2)]. The ε' and ε'' of Ti_2CT_X/Si_3N_4 aerogel with layered biomimetic structure exhibited a similar trend at 8.2-10.2 GHz. In this frequency range, ε' decreases from 2.6 to 2.3, while ε'' decreases from 2.2 to 1.8. In the 9.6-10.2 GHz frequency range, ε' increases slightly, and ε_r shows an overall decreasing trend with increasing frequency, which is related to the frequency dispersion effect and caused by polarization relaxation. When the electric field frequency is too high, the dipole cannot align with the electric field for a short period. This leads to weak polarization relaxation and consequently a decrease in the dielectric constant. The μ' and μ'' of Ti_2CT_X/Si_3N_4 aerogel are 0 and 1, respectively [Supplementary Figure 5], indicating that the aerogel is non-magnetic. Generally, excellent electromagnetic wave absorption performance depends primarily on the dielectric and magnetic losses of the material. For non-magnetic Ti_2CT_X/Si_3N_4 aerogels, electromagnetic wave absorption mainly depends on dielectric loss. The ε' and ε'' of

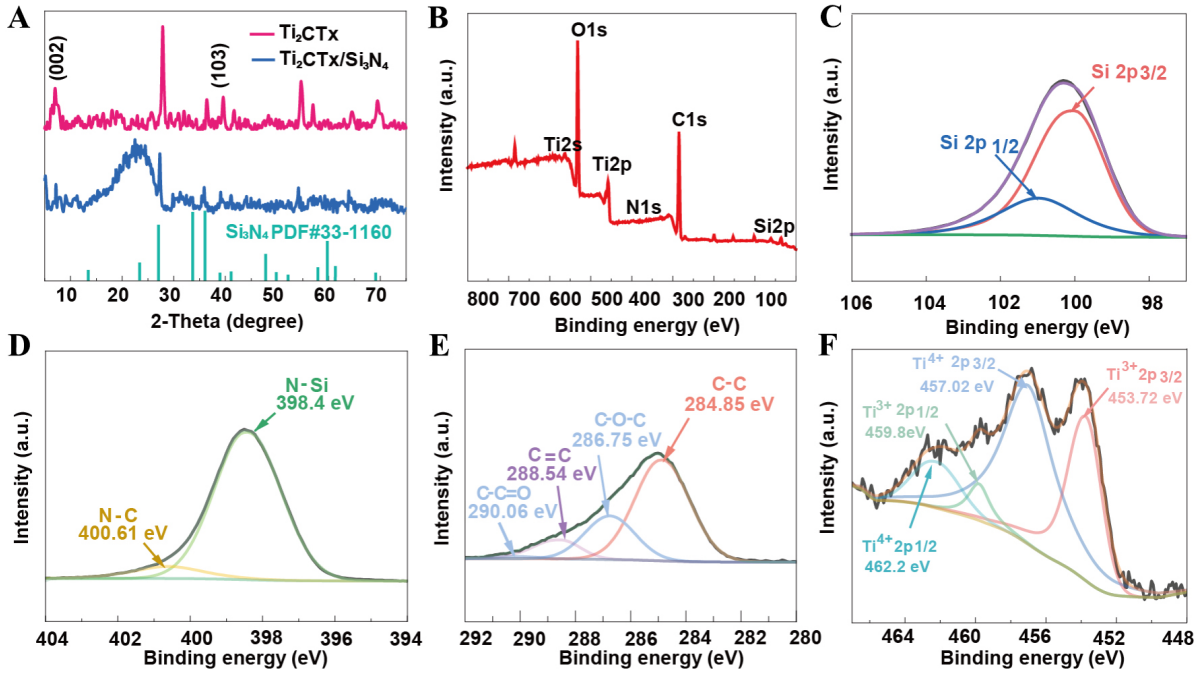

Figure 4. Microstructure of Ti_2CT_X and Ti_2CT_X/Si_3N_4. (A) The XRD images of Ti_2CT_X and Ti_2CT_X/Si_3N_4; (B)The XPS images of Ti_2CT_X/Si_3N_4; (C) Si 2p XPS spectra; (D) N 1s XPS spectra; (E) C 1s XPS spectra; (F) Ti 2p XPS spectra. XRD: X-ray diffraction; XPS: X-ray photoelectron spectroscopy.

aerogels with unidirectional porous structure gradually decrease between 8.2 and 12.4 GHz [Figure 5B(2)]. The real part decreases from 1.2 to 0.6, and the imaginary part decreases from 0.9 to 0.3. Comparing the dielectric constants of the two structures reveals that the real and imaginary parts of the layered biomimetic Ti_2CT_X/Si_3N_4 aerogel structure are greater than those of the porous structure.

Reflection loss (RL) is an important parameter that directly reflects wave absorption performance. RL less than -10 dB usually indicates that more than 90% of the incident electromagnetic wave can be absorbed, with the corresponding frequency range being the EAB. RL less than -20 dB usually indicates that more than 99% of the electromagnetic wave can be absorbed. RL can be less than -10 dB within a thickness range of 4.7-8 mm, frequency in the range of 8-12.4 GHz, enabling effective electromagnetic wave absorption [Figure 5A(3) and Supplementary Figure 6]. The RL of Ti_2CT_X/Si_3N_4 aerogel increases and then decreases as the thickness increases [Figure 5A(4)]. It can be seen that RL reaches -53 dB and the EAB is up to 4.2 GHz at 10.8 GHz with a thickness of 5 mm, which covers the whole X-band. There are no effective absorption peaks or EAB when the thickness is between 4 and 7.5 mm [Figure 5B(3)]. The RL of porous aerogel increases with thickness [Figure 5B(4)]. When the thickness is 10 mm, the minimum RL is -20 dB, which can cover the X band [Supplementary Figure 7]. To illustrate the electromagnetic wave absorption properties in real far-field conditions, the radar cross section (RCS) of the samples is calculated. The RCS of the 5 mm thick Ti_2CT_X/Si_3N_4 aerogel is less than -20 dB at different frequencies [Figure 5C] and different angles [Supplementary Figure 8] indicating its potential for practical applications, for example, the RCS is -26.63 dB at 8.2 GHz, -26.40 dB at 10.3 GHz, and -26.39 dB at 12.4 GHz, which enables 99% absorption of electromagnetic waves.

To evaluate the dielectric loss capability, the tangent of the dielectric loss was calculated based on the dielectric parameters [Figure 6A]. Within the 8.2-12.4 GHz frequency range, the tangent loss of the layered

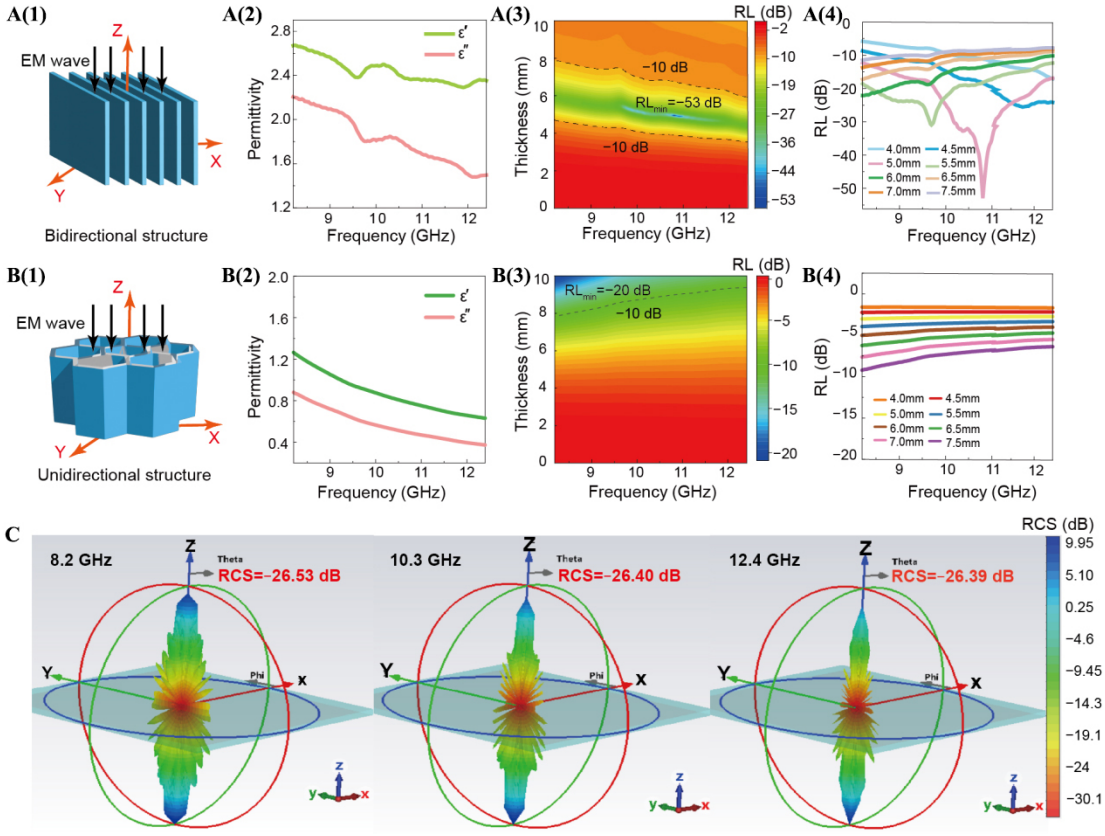

Figure 5. Dielectric and microwave absorbing properties of Ti_2CT_X/Si_3N_4. (A1) Bidirectional structure: electromagnetic waves are incident along the Z-axis; (A2) The ε' and ε'' of Bidirectional structure; (A3) The 3D RL values of Bidirectional structure; (A4) RL of Bidirectional structure at different thicknesses; (B1) Unidirectional structure: electromagnetic waves are incident along the Z-axis; (B2) The ε' and ε'' of Unidirectional structure; (B3) The three-dimensional RL values of Unidirectional structure; (B4) RL of Unidirectional structure at different thicknesses; (C) Three-dimensional radar wave scattering signals of Ti_2CT_X/Si_3N_4. 3D: three-dimensional; RL: reflection loss.

biomimetic structure ranged from 0.82 to 0.63, and that of the porous structure ranged from 0.69 to 0.56. Distinct peaks in the dielectric loss tangent of the bidirectional structure appear at 9.5 GHz and 10.5 GHz [Figure 6A]. These maxima arise from a synergistic resonance between dipolar polarization (from -OH, -F, and other functional groups on Ti_2CT_X) and interfacial polarization at the low-dielectric Si_3N_4 interface[61]. The attenuation coefficient refers to the ability of electromagnetic waves to be attenuated when entering a material[62,63]. Ti_2CT_X/Si_3N_4 aerogel with a biomimetic layered structure has a better attenuation coefficient from 100-120 at 8.2-12.4 GHz [Figure 6B], and the attenuation coefficient increases overall with increasing frequency. Aerogel with a porous structure has an attenuation coefficient about 60 at 8.2-12.4 GHz, this indicates that electromagnetic waves are effectively dissipated in the Ti_2CT_X interlayer. Excellent electromagnetic wave absorption performance can only be achieved by having suitable impedance matching and strong attenuation capability at the same time. Impedance matching ($Z = Z_i/Z_0$) determines whether the electromagnetic wave can enter the material system; impedance matching is better when Z is closer to 1[64,65]. Introducing electromagnetic wave transparent Si_3N_4 allows electromagnetic waves to enter the interior of the material rather than being reflected at the surface, effectively optimizing the impedance matching of Ti_2CT_X. For the bidirectional structure, Z remains within 0.4-1.2 across the entire 8.2-12.4 GHz band and stays very close to the ideal value of 1 for all investigated thicknesses [Figure 6C]. By contrast, the unidirectional structure exhibits Z in the range 0.8-3 over the same frequency range, progressively deviating from 1 as thickness increases [Supplementary Figure 9]. The superior impedance matching in the

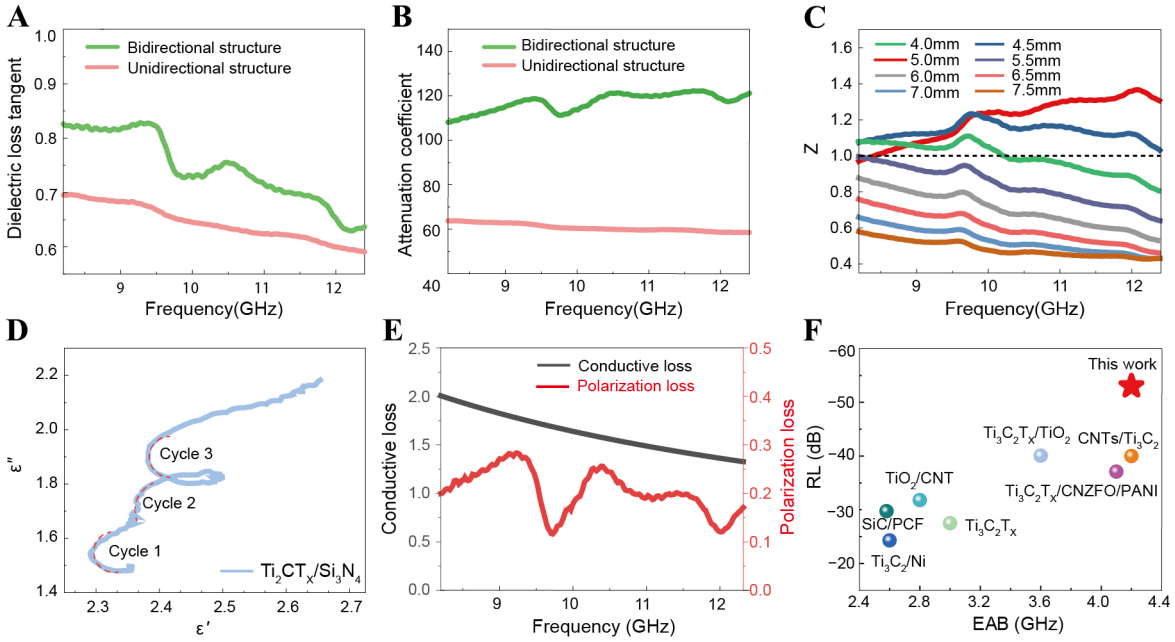

Figure 6. Ti_2CT_X/Si_3N_4 microwave-absorption mechanism. (A) The dielectric loss tangent of different structures; (B) The attenuation coefficient of different structures, (C) The Z values of Ti_2CT_X/Si_3N_4; (D) The cole-cole curve of Ti_2CT_X/Si_3N_4; (E) The calculated conductive loss and polarization loss; (F) Comparison of EAB and RL of Ti_2CT_X/Si_3N_4 aerogel with the reported literature. EAB: Effective absorption bandwidth; RL: reflected loss.

bidirectional structure originates from the graded-index transition enabled by the low-permittivity Si_3N_4 outer layers, which markedly mitigates the abrupt impedance mismatch between air and the highly conductive Ti_2CT_X layers.

According to the Debye theory, the dielectric behavior of Ti_2CT_X/Si_3N_4 aerogels can be evaluated using Cole-Cole curves[66]. The relationship between ε' and ε'' is semicircular, with each semicircle representing a Debye relaxation process. The relationship between ε' and ε'' of Ti_2CT_X/Si_3N_4 aerogel shows multiple distorted semicircles [Figure 6D], implying the existence of multiple modes of polarization loss. The curves in Figure 6D show multiple twisted semicircles, which implies the existence of multiple modes of polarization loss. These multiple relaxation processes may originate from dipole and interface polarization. Functional groups, structural defects, and a disordered lattice can act as dipole centers, inducing the generation of dipole polarization in an alternating electromagnetic field. Additionally, the heterogeneous junction surface between Ti_2CT_X and Si_3N_4 facilitates polarization loss at the interface. The Cole-Cole curve of the Ti_2CT_X/Si_3N_4 aerogel is straight in the low-frequency region, which is related to conductive loss and may originate from the excellent electrical conductivity of Ti_2CT_X[67]. As the Ti_2CT_X/Si_3N_4 aerogel is non-magnetic, its attenuation ability mainly depends on conductive and polarization losses, with the conductive loss being the dominant factor [Figure 6E].

When compared with other MXene-based electromagnetic wave absorbing materials, the Ti_2CT_X/Si_3N_4 aerogel produced in this study exhibits significant advantages [Figure 6F], including a broad EAB and robust absorption properties.

The electromagnetic wave absorbing mechanism of the prepared Ti_2CT_X/Si_3N_4 aerogel mainly includes the following [Supplementary Figure 10]: (1) Interfacial polarization loss: The abundant surface functional

groups on Ti_2CT_X, combined with the low dielectric constant of Si_3N_4 [Supplementary Table 3], work synergistically at the Ti_2CT_X/Si_3N_4 interface. The significant disparity in electrical conductivity and dielectric constant between the two materials leads to intense charge accumulation and rearrangement under an electric field, resulting in the formation of macroscopic electric dipole moments[68]. This loss mechanism converts electromagnetic wave energy into thermal energy via polarization relaxation, thereby achieving effective absorption of electromagnetic waves. Additionally, the interfacial polarization between Ti_2CT_X and Si_3N_4 significantly enhanced the electromagnetic wave-absorbing properties of the composite; (2) Multiple reflections and scattering: the layered porous structure of the Ti_2CT_X/Si_3N_4 aerogel promotes multiple reflections and scattering of electromagnetic waves within the material[69]. This structural design significantly increases the propagation path of electromagnetic waves[70], thereby improving their energy dissipation efficiency; (3) Impedance matching: The low-dielectric-constant Si_3N_4 outer layers form a graded-index transition zone[71], which significantly mitigates the abrupt impedance mismatch between air and the highly conductive Ti_2CT_X layers, thereby markedly reducing surface reflection and increasing the depth of electromagnetic wave penetration and absorption efficiency[72]; (4) Synergistic effect: Ti_2CT_X exhibits high electrical conductivity. The conductive network formed by Ti_2CT_X nanosheets provides pathways for electron migration, generating conduction currents that dissipate electromagnetic wave energy through a conductive loss mechanism[33]. When Ti_2CT_X is compounded with Si_3N_4, this mechanism is retained and enhanced by the structural optimization of Si_3N_4. The combination of the high electrical conductivity of Ti_2CT_X and the low dielectric constant of Si_3N_4 results in an efficient electromagnetic wave absorption system[73-75].

Mechanical properties of Ti_2CT_X/Si_3N_4 aerogel with bidirectional structure

The freeze-dried Ti_2CT_X/Si_3N_4 aerogel possesses a porous structure that results in a low density. This allows it to be easily placed on plant leaves without significantly bending them [Supplementary Figure 11A]. The combination of the aerogel's anisotropic porous structure and the deposited Si_3N_4 imparts considerable strength to the Ti_2CT_X/Si_3N_4 aerogels. This enables the aerogel to sustain multiple times its own weight without fracturing [Supplementary Figure 11B]. When a maximum compressive force of 15.69 kN was applied, the compressive modulus of elasticity was found to be 14.56 GPa, while the compressive strength was found to be 315 MPa. This indicates that the Ti_2CT_X/Si_3N_4 aerogel has excellent mechanical properties [Supplementary Figure 11B]. Moreover, we investigated the high-temperature stability of Ti_2CT_X/Si_3N_4 aerogel further by testing their thermogravimetric curves in air or Ar atmospheres, respectively. In an air atmosphere, the weight loss begins at 400 °C and plateaus at 1,200 °C, with a loss of only 1.25% [Supplementary Figure 11C]. In an Ar atmosphere, the weight loss was 1.75% at 1,200 °C [Supplementary Figure 11D]. The quality of the Ti_2CT_X/Si_3N_4 aerogel remained above 98% in different atmospheres, demonstrating its excellent thermal stability.

CONCLUSIONS

In summary, Ti_2CT_X aerogel with aligned lamellar porous structure was prepared using a bidirectional freeze-drying process. Subsequently, amorphous Si_3N_4 was infiltrated into the Ti_2CT_X using the Chemical Vapor Infiltration technique to produce a bionic, porous Ti_2CT_X/Si_3N_4 aerogel with an intercalated lamellar structure. The experimental results show that, with a Ti_2CT_X concentration of just 0.21 wt.%, the Ti_2CT_X/Si_3N_4 composite exhibits an EAB spanning the entire X-band (8.2-12.4 GHz). This is achieved with a minimum reflection loss of -53 dB at a thickness of 5 mm. The microwave absorption mechanism of Ti_2CT_X/Si_3N_4 is attributed to multiple polarizations at the heterojunction interface and multiple reflections and conductive losses between Ti_2CT_X layers. Meanwhile, the Ti_2CT_X/Si_3N_4 composites prepared show advantages in terms of their lightweight properties, robust mechanical properties, and high-temperature stability, providing important insights for the application of Ti_2CT_X in nano-electromagnetic engineering, especially in the field of electromagnetic pollution mitigation.

DECLARATIONS

Acknowledgments

We are grateful to Gao Qianwen (Analytical & Testing Center of NPU) for her help in the microstructure characterization.

Authors' contributions

Wrote the original draft: Xu, H.; Jing, C.; Xu, Z.; Zhan, H.
Supervised, reviewed, and revised the manuscript: Ye, F.; Chen, Q.; Zhu, M.; Kong, L.; Li, X.; Chai, X.; Qing, Y.; Fan, X.; Luo, F.

Availability of data and materials

The data that support the findings of this study are available from the corresponding author upon reasonable request.

Financial support and sponsorship

This work was supported by the National Natural Science Foundation of China (Grants Nos. 52302367, 52203094), the National Key Laboratory of Electromagnetic Information Control and Effects Open Fund (Grants No. SYS1W2023010304), and the State Key Laboratory of Solidification Processing in NPU (Grant No. 2025-TS-08).

Conflict of Interest

Xia Chai is affiliated with Shaanxi Huaqin Technology Industry Co., Ltd, while the other authors have declared that they have no conflicts of interest.

Ethical approval and consent to participate

Not applicable.

Consent for publication

Not applicable.

REFERENCES

1. Wu, Z.; Cheng, H.; Jin, C.; et al. Dimensional design and core-shell engineering of nanomaterials for electromagnetic wave absorption. *Adv. Mater.* **2022**, *34*, 2107538. DOI
2. Qin, M.; Zhang, L.; Wu, H. Dielectric loss mechanism in electromagnetic wave absorbing materials. *Adv. Sci. (Weinh).* **2022**, *9*, 2105553. DOI PubMed PMC
3. Lv, H.; Yao, Y.; Yuan, M.; et al. Functional nanoporous graphene superlattice. *Nat. Commun.* **2024**, *15*, 1295. DOI PubMed PMC
4. Zhang, Y.; Liu, A.; Tian, Y.; et al. Direct-ink-writing printed aerogels with dynamically reversible thermal management and tunable electromagnetic interference shielding. *Adv. Mater.2025*, 2505521. DOI
5. Liu, A.; Qiu, H.; Lu, X.; et al. Asymmetric structural MXene/PBO aerogels for high-performance electromagnetic interference shielding with ultra-low reflection. *Adv. Mater.* **2024**, *37*, 2414085. DOI
6. Liu, Y.; Zhou, J.; Li, C.; et al. Interfacial coupling effects in two-dimensional ordered arrays for microwave attenuation. *Nat. Commun.* **2025**, *16*, 202. DOI PubMed PMC
7. Yuan, L.; Zhao, T.; Dai, J.; et al. High-density, crosstalk-free, flexible electrolyte-gated synaptic transistors array via all-photolithography for multimodal neuromorphic computing. *Adv. Funct. Mater.* **2025**, *35*, 2418052. DOI
8. Cheng, S.; Sheng, D.; Mukherjee, S.; et al. Carbon nanolayer-mounted single metal sites enable dipole polarization loss under electromagnetic field. *Nat. Commun.* **2024**, *15*, 9077. DOI PubMed PMC
9. Tao, J.; Yan, Y.; Zhou, J.; et al. Anionic high-entropy doping engineering for electromagnetic wave absorption. *Nat. Commun.* **2025**, *16*, 3163. DOI PubMed PMC

10. Liu, L.; Deng, H.; Tang, X.; et al. Specific electromagnetic radiation in the wireless signal range increases wakefulness in mice. *Proc. Natl. Acad. Sci. U. S. A.* **2021**, *118*, e2105838118. DOI PubMed PMC
11. Gulati, S.; Yadav, A.; Kumar, N.; Priya, K.; Aggarwal, N. K.; Gupta, R. Phenotypic and genotypic characterization of antioxidant enzyme system in human population exposed to radiation from mobile towers. *Mol. Cell. Biochem.* **2017**, *440*, 1-9. DOI
12. Han, Y.; Guo, H.; Qiu, H.; et al. Multimechanism decoupling for low-frequency microwave absorption hierarchical Fe-doped Co magnetic microchains. *Adv. Funct. Mater.2025*, 2506803. DOI
13. Zhou, L.; Hu, P.; Bai, M.; et al. Harnessing the electronic spin states of single atoms for precise electromagnetic modulation. *Adv. Mater.* **2024**, *37*, 2418321. DOI
14. Ma, Z.; Xiang, X.; Shao, L.; Zhang, Y.; Gu, J. Multifunctional wearable silver nanowire decorated leather nanocomposites for joule heating, electromagnetic interference shielding and piezoresistive sensing. *Angew. Chem. Int. Ed. Engl.* **2022**, *61*, e202200705. DOI
15. Li, X.; Sheng, X.; Guo, Y.; et al. Multifunctional HDPE/CNTs/PW composite phase change materials with excellent thermal and electrical conductivities. *J. Mater. Sci. Technol.* **2021**, *86*, 171-9. DOI
16. Wegst, U. G. K.; Bai, H.; Saiz, E.; Tomsia, A. P.; Ritchie, R. O. Bioinspired structural materials. *Nat. Mater.* **2014**, *14*, 23-36. DOI PubMed
17. Dang, X.; Yi, H.; Ham, M. H.; et al. Virus-templated self-assembled single-walled carbon nanotubes for highly efficient electron collection in photovoltaic devices. *Nat. Nanotechnol.* **2011**, *6*, 377-84. DOI
18. Chen, Y.; Zheng, Y.; Zhou, Y.; et al. Multi-layered cement-hydrogel composite with high toughness, low thermal conductivity, and self-healing capability. *Nat. Commun.* **2023**, *14*, 3438. DOI PubMed PMC
19. Zhai, M.; Zhao, S.; Guo, H.; et al. Bionic-structured electromagnetic interference shielding composites. *Sci. Bull. (Beijing).* **2025**, *70*, 2347-64. DOI
20. Wang, B.; Ni, C.; Ding, M.; et al. Hierarchically pepper wood-like Co_3Fe_7@C nanotubes for broadband microwave absorption and efficient electromagnetic interference shielding. *J. Mater. Sci. Technol.* **2026**, *244*, 196-207. DOI
21. Cammarata, M.; Nicoletti, F.; Di, P. M.; Valenza, A.; Zummo, G. Mechanical behavior of human bones with different saturation levels. In: 2nd International Electronic Conference on Materials: Proceedings of the 2nd International Electronic Conference on Materials; 2016 May 2-16; Online. Basel: MDPI; 2016. p. B003. DOI
22. Xu, H.; Zhan, H.; Xu, Z.; et al. Sandwich-like CNTs/Carbon@Si_3N_4 porous foam for temperature-insensitive electromagnetic wave absorption. *Adv. Funct. Mater.* **2025**, *35*, 2421242. DOI
23. Wei, C.; Shi, L.; Li, M.; et al. Hollow engineering of sandwich NC@Co/NC@MnO_2 composites toward strong wideband electromagnetic wave attenuation. *J. Mater. Sci. Technol.* **2024**, *175*, 194-203. DOI
24. Zhang, Y.; Ruan, K.; Gu, J. Flexible sandwich-structured electromagnetic interference shielding nanocomposite films with excellent thermal conductivities. *Small.* **2021**, *17*, 2101951. DOI PubMed
25. Lakes, R. Materials with structural hierarchy. *Nature.* **1993**, *361*, 511-5. DOI
26. Ajdary, R.; Tardy, B. L.; Mattos, B. D.; Bai, L.; Rojas, O. J. Plant nanomaterials and inspiration from nature: water interactions and hierarchically structured hydrogels. *Adv. Mater.* **2020**, *33*, 2001085. DOI PubMed PMC
27. Chen, Z.; Zhang, Y.; Wang, Z.; et al. Bioinspired moth-eye multi-mechanism composite ultra-wideband microwave absorber based on the graphite powder. *Carbon.* **2023**, *201*, 542-8. DOI
28. Zheng, J.; Lan, D.; Zhang, S.; et al. Zeolite imidazolate framework derived efficient absorbers: From morphology modulation to component regulation. *J. Alloys. Compd.* **2025**, *1010*, 177092. DOI
29. Xiao, J.; Zhan, B.; He, M.; et al. Interfacial polarization loss improvement induced by the hollow engineering of necklace-like PAN/carbon nanofibers for boosted microwave absorption. *Adv. Funct. Mater.* **2024**, *35*, 2316722. DOI
30. Zhang, Y.; Ruan, K.; Zhou, K.; Gu, J. Controlled distributed $Ti_3C_2T_x$ hollow microspheres on thermally conductive polyimide composite films for excellent electromagnetic interference shielding. *Adv. Mater.* **2023**, *35*, 2211642. DOI
31. Zhao, R.; Gao, T.; Li, Y.; et al. Highly anisotropic Fe_3C microflakes constructed by solid-state phase transformation for efficient microwave absorption. *Nat. Commun.* **2024**, *15*, 1497. DOI PubMed PMC
32. Zhou, Y.; Zhang, Y.; Ruan, K.; et al. MXene-based fibers: preparation, applications, and prospects. *Sci. Bull. (Beijing).* **2024**, *69*, 2776-92. DOI
33. Wang, B.; Ni, C.; Xie, X.; Ding, M.; Li, C. Carbon nanotubes-encapsulated Co/Co_7Fe_3 nanocomposites: achieving wideband electromagnetic wave absorption at ultrathin-thickness by regulating magnetic phase ratio. *Chem. Eng. J.* **2024**, *494*, 153076. DOI
34. Li, X.; Niu, M.; Li, C.; et al. Dipole polarization and synchronous magnetic modulation induced by FeN_4 moiety on $Ti_3C_2T_x$ for superior electromagnetic wave absorption performance. *Carbon. Energy.2025*, e70078. DOI
35. Zhang, Y.; Ruan, K.; Guo, Y.; Gu, J. Recent Advances of MXenes-based optical functional materials. *Adv. Photonics. Res.* **2023**, *4*, 2300224. DOI
36. Sun, Y.; Su, Y.; Chai, Z.; Jiang, L.; Heng, L. Flexible solid-liquid Bi-continuous electrically and thermally conductive nanocomposite for electromagnetic interference shielding and heat dissipation. *Nat. Commun.* **2024**, *15*, 7290. DOI PubMed PMC
37. Zhang, Y.; Yan, Y.; Qiu, H.; Ma, Z.; Ruan, K.; Gu, J. A mini-review of MXene porous films: Preparation, mechanism and application. *J. Mater. Sci. Technol.* **2022**, *103*, 42-9. DOI
38. Zhou, Y.; Zhang, Y.; Pang, Y.; et al. Thermally conductive $Ti_3C_2T_x$ fibers with superior electrical conductivity. *Nanomicro. Lett.* **2025**, *17*, 235. DOI PubMed PMC
39. Du, Z.; Yang, S.; Li, S.; et al. Conversion of non-van der Waals solids to 2D transition-metal chalcogenides. *Nature.* **2020**, *577*, 492-6.

DOI

40. Murali, G.; Reddy, M. J. K.; Park, Y. H.; et al. A review on MXene synthesis, stability, and photocatalytic applications. *ACS. Nano.* **2022**, *16*, 13370-429. DOI
41. Xie, W.; Tang, Q.; Xie, J.; et al. Organohydrogel-based transparent terahertz absorber via ionic conduction loss. *Nat. Commun.* **2024**, *15*, 38. DOI PubMed PMC
42. Jiang, H.; Yuan, B.; Guo, H.; et al. Malleable, printable, bondable, and highly conductive MXene/liquid metal plasticine with improved wettability. *Nat. Commun.* **2024**, *15*, 6138. DOI PubMed PMC
43. Zhao, S.; Zhang, H. B.; Luo, J. Q.; et al. Highly electrically conductive three-dimensional $Ti_3C_2T_c$ MXene/reduced graphene oxide hybrid aerogels with excellent electromagnetic interference shielding performances. *ACS. Nano.* **2018**, *12*, 11193-202. DOI
44. Wu, X.; Wang, Z.; Yu, M.; Xiu, L.; Qiu, J. Stabilizing the MXenes by carbon nanoplating for developing hierarchical nanohybrids with efficient lithium storage and hydrogen evolution capability. *Adv. Mater.* **2017**, *29*, 1607017. DOI
45. Ma, T. B.; Ma, H.; Ruan, K. P.; et al. Thermally conductive poly(lactic acid) composites with superior electromagnetic shielding performances via 3D printing technology. *Chin. J. Polym. Sci.* **2022**, *40*, 248-55. DOI
46. Lin, Y.; Tang, L.; Cheng, L.; et al. Mechanically strong PBO wave-transparent composite papers with excellent UV resistance and ultra-low dielectric constant. *J. Mate. Sci. Technol.* **2025**, *225*, 151-8. DOI
47. Lin, Y.; Yong, Z.; Luo, X.; et al. Monolithically integrated, broadband, high-efficiency silicon nitride-on-silicon waveguide photodetectors in a visible-light integrated photonics platform. *Nat. Commun.* **2022**, *13*, 6362. DOI PubMed PMC
48. Bauters, J. F.; Heck, M. J. R.; John, D.; et al. Ultra-low-loss high-aspect-ratio Si_3N_4 waveguides. *Opt. Express.* **2011**, *19*, 3163. DOI
49. Ding, M.; Zhao, D.; Wei, R.; et al. Multifunctional elastomeric composites based on 3D graphene porous materials. *Exploration. (Beijing).* **2023**, *4*, 20230057. DOI
50. Wang, H.; Zhao, J.; Wang, Z.; Liu, P. Bird-nest-like multi-interfacial MXene@SiC_{NWs}@Co/C hybrids with enhanced electromagnetic wave absorption. *ACS. Appl. Mater. Interfaces.* **2023**, *15*, 4580-90. DOI
51. Wang, L.; Chen, Z.; Wang, X.; et al. Fe_3O_4@C 3D foam for strong low-frequency microwave absorption. *J. Materiomics.* **2023**, *9*, 148-56. DOI
52. Wang, D.; Zhou, C.; Filatov, A. S.; et al. Direct synthesis and chemical vapor deposition of 2D carbide and nitride MXenes. *Science.* **2023**, *379*, 1242-7. DOI
53. Chen, X.; Park, Y. J.; Kang, M.; et al. CVD-grown monolayer MoS_2 in bioabsorbable electronics and biosensors. *Nat. Commun.* **2018**, *9*, 1690. DOI PubMed PMC
54. Wang, W.; Chen, S. J.; Chen, W.; Duan, W.; Lai, J. Z.; Sagoe-crentsil, K. Damage-tolerant material design motif derived from asymmetrical rotation. *Nat. Commun.* **2022**, *13*, 1289. DOI PubMed PMC
55. Zhang, J.; Liu, Z.; Han, M.; Zhang, J.; Tang, Y.; Gu, J. Block copolymer functionalized quartz fibers/cyanate ester wave-transparent laminated composites. *J. Mater. Sci. Technol.* **2023**, *139*, 189-97. DOI
56. Ma, X.; Zhang, H.; Guo, Y.; et al. Enhancing thermal conductivity in polysiloxane composites through synergistic design of liquid crystals and boron nitride nanosheets. *J. Mater. Sci. Technol.* **2025**, *231*, 54-61. DOI
57. Liu, X.; Zhang, L.; Liu, Y.; Ye, F.; Yin, X. Thermodynamic calculations on the chemical vapor deposition of Si-C-N from the $SiCl_4$-NH_3-C_3H_6-H_2-Ar system. *Ceram. Int.* **2013**, *39*, 3971-7. DOI
58. Gao, C.; He, X.; Ye, F.; Wang, S.; Zhang, G. Electromagnetic wave absorption and mechanical properties of CNTs@GN@Fe_3O_4/PU multilayer composite foam. *Materials. (Basel).* **2021**, *14*, 7244. DOI PubMed PMC
59. Pang, X.; Zhou, X.; Gao, Y.; Qian, Y.; Lyu, L. Optimization of electromagnetic absorption properties based on graphene, carbon nanotubes, and multidimensional composites. *Polym. Compos.* **2024**, *45*, 8414-25. DOI
60. Cai, H.; Lin, Z.; Gao, L.; Feng, C.; Tang, R. Non-magnetic hollow ZnO/C fabricated by a novel ZnO self-sacrificial template hollow engineering for efficient microwave absorption. *J. Mater. Sci.* **2024**, *59*, 5371-86. DOI
61. Pan, Y.; Cheng, L.; Lan, D.; et al. Conductor-semiconductor heterointerface polarization enhancement for superior electromagnetic wave absorption. *J. Mater. Sci. Technol.* **2026**, *244*, 129-41. DOI
62. Gao, X.; Wang, X.; Cai, J.; et al. CNT cluster arrays grown on carbon fiber for excellent green EMI shielding and microwave absorbing. *Carbon.* **2023**, *211*, 118083. DOI
63. Ma, W.; He, P.; Wang, T.; et al. Microwave absorption of carbonization temperature-dependent uniform yolk-shell H-Fe_3O_4@C microspheres. *Chem. Eng. J.* **2021**, *420*, 129875. DOI
64. Liu, X. H.; Cai, J. N.; Zhang, J. Y.; et al. Surface-state-constrained topological insulator Bi_2Te_3 nanorods for electromagnetic wave trapping and conversion into electricity. *J. Mater. Sci. Technol.* **2026**, *244*, 149-55. DOI
65. Hou, Z. L.; Gao, X.; Zhang, J.; Wang, G. A perspective on impedance matching and resonance absorption mechanism for electromagnetic wave absorbing. *Carbon.* **2024**, *222*, 118935. DOI
66. Zhang, X.; Xu, L.; Zhou, J.; et al. Liquid metal-derived two-dimensional layered double oxide nanoplatelet-based coatings for electromagnetic wave absorption. *ACS. Appl. Nano. Mater.* **2021**, *4*, 9200-12. DOI
67. Gu, W.; Luo, Z.; Wang, J.; et al. Multifunctional lightweight rGO/polyimide hybrid aerogels for highly efficient infrared-radar-acoustic compatibility via heterogeneous interface engineering strategies. *J. Mater. Sci. Technol.* **2026**, *243*, 102-14. DOI
68. Zhu, M.; Chen, W.; Lei, Y.; et al. Lightweight porous aerogels comprising nanofibrillated cellulose and MXene nanosheets for simultaneous microwave and sound absorption applications. *ACS. Appl. Nano. Mater.* **2025**, *8*, 3584-94. DOI
69. Kong, L.; Zhang, G.; Cui, H.; Qi, J.; Wang, T.; Xu, H. Deformation induced absorption band-tunable smart CNTs/$Ti_3C_2T_x$-WPU

electromagnetic wave absorbing aerogel. *Carbon.* **2024**, *223*, 119023. DOI

70. Kong, L.; Zhang, S.; Liu, Y.; Xu, H.; Fan, X.; Huang, J. Flexible CNTs/CNF-WPU aerogel for smart electromagnetic wave absorbing with tuning effective absorption bandwidth. *Carbon.* **2023**, *207*, 13-22. DOI
71. Jing, L.; Luo, F.; Xu, H.; Wang, C.; Pan, H. Mechanically robust Al_2O_{3f}/$LaPO_4$/Al_2O_3 composite for high-performance microwave transparent. *J. Alloys. Compd.* **2025**, *1010*, 177974. DOI
72. Guo, S.; Zhang, J.; Lin, C.; Ge, J.; Bi, S.; Hou, Z. L. Multilayer core-shell structured $FeNi_3$@C with enhanced interfacial polarization for microwave absorbers. *Nano. Res.* **2025**, *18*, 94907151. DOI
73. Wang, H.; Guo, J.; Lei, Y.; et al. Stable and transparent Ca^{2+}-cross-linked alginate composite films for EMI shielding and joule heating. *ACS. Appl. Nano. Mater.* **2024**, *7*, 2100-9. DOI
74. Tang, Z.; Xu, L.; Xie, C.; et al. Synthesis of $CuCo_2S_4$@expanded graphite with crystal/amorphous heterointerface and defects for electromagnetic wave absorption. *Nat. Commun.* **2023**, *14*, 5951. DOI PubMed PMC
75. Xu, Z.; Zhan, H.; Jing, C.; et al. Scalable liquid-phase synthesis of core-shell absorbers: Synergistic dielectric/magnetic losses dominating microwave attenuation. *Nano. Res.* **2025**, [Accepted]. DOI